Cell division plane orientation based on tensile stress inArabidopsis thaliana

Marion Louveaux, Jean-Daniel Julien, Vincent Mirabet, Arezki Boudaoud, Arezki Boudaoud, Olivier O. Hamant

Cell division plane orientation based on tensile stress in *Arabidopsis thaliana*

Marion Louveaux[a,b], Jean-Daniel Julien[a,b,c], Vincent Mirabet[a,b], Arezki Boudaoud[a,b,1], and Olivier Hamant[a,b,1]

[a]Laboratoire Reproduction et Développement des Plantes, Université de Lyon, Ecole Normale Supérieure (ENS) de Lyon, Université Claude Bernard (UCB) Lyon 1, CNRS, Institut National de la Recherche Agronomique, F-69342 Lyon, France; [b]Laboratoire Joliot-Curie, CNRS, ENS de Lyon, UCB Lyon 1, Université de Lyon, 69364 Lyon, Cedex 07, France; and [c]Laboratoire de Physique, CNRS, ENS de Lyon, UCB Lyon 1, Université de Lyon, 69364 Lyon, Cedex 07, France

Edited by Richard Scott Poethig, University of Pennsylvania, Philadelphia, PA, and approved May 23, 2016 (received for review January 14, 2016)

Cell geometry has long been proposed to play a key role in the orientation of symmetric cell division planes. In particular, the recently proposed Besson–Dumais rule generalizes Errera's rule and predicts that cells divide along one of the local minima of plane area. However, this rule has been tested only on tissues with rather local spherical shape and homogeneous growth. Here, we tested the application of the Besson–Dumais rule to the divisions occurring in the *Arabidopsis* shoot apex, which contains domains with anisotropic curvature and differential growth. We found that the Besson–Dumais rule works well in the central part of the apex, but fails to account for cell division planes in the saddle-shaped boundary region. Because curvature anisotropy and differential growth prescribe directional tensile stress in that region, we tested the putative contribution of anisotropic stress fields to cell division plane orientation at the shoot apex. To do so, we compared two division rules: geometrical (new plane along the shortest path) and mechanical (new plane along maximal tension). The mechanical division rule reproduced the enrichment of long planes observed in the boundary region. Experimental perturbation of mechanical stress pattern further supported a contribution of anisotropic tensile stress in division plane orientation. Importantly, simulations of tissues growing in an isotropic stress field, and dividing along maximal tension, provided division plane distributions comparable to those obtained with the geometrical rule. We thus propose that division plane orientation by tensile stress offers a general rule for symmetric cell division in plants.

cell division plane | mechanical forces | meristem | vertex model | *Arabidopsis*

Regulation of cell division plane orientation is a way for multicellular organisms to control the topology (number of adjacent cells) and geometry (cell shapes and sizes) of their tissues, as illustrated in simulations of growing tissue under different division rules (for instance, ref. 1). Whereas this process may be compensated by cell death and cell rearrangement in animal tissues, such compensation may occur only through subsequent growth patterns in plants: Plant cells are glued to each other by stiff pectocellulosic cell walls, which prevent cell movement, and cell death usually does not occur in young, rapidly dividing tissues. Mechanically, the creation of a new cell wall also leads to the local reinforcement of the tissue in a preferential direction. Altogether, this raises the question of the cues that help in controlling cell division plane orientation in plants.

At the end of the 19th century, Hofmeister (2), Sachs (3), and Errera (4) proposed that cell division plane orientation in symmetric divisions only relies on cell geometry. In particular, Léo Errera originally observed that cells behave like soap bubbles when positioning their division plane; i.e., they tend to minimize the area of the new interface between the two daughter cells. From this statement was derived the now famous Errera's rule, "cells divide along the shortest path," which is a rough simplification of Errera's initial observation (for a full review, see ref. 5). Errera's rule was able to recapitulate the development of a simple organism like *Coleochaete orbicularis*, albeit with some level of noise (6). These geometric rules were also tested in the *Arabidopsis* shoot apical meristem (SAM), a dome-shaped group of dividing cells that generates every aerial organ. Although Errera's rule described the highest percentage of divisions, neither Hofmeister's, nor Errera's, nor Sachs' rules fully described all of the divisions at the SAM (7).

Recently, Errera's original statement was elegantly reexamined through an analogy with soap bubbles: Cells do not always divide along the shortest path, but instead divide along one of the shortest paths (5). Indeed, for a given cell geometry, several minima of path length exist and the probability to divide along one of these minima is related to the area of the interface between the two daughter cells. Based on these observations, the deterministic "shortest path" rule was generalized to a probabilistic one, referred to here as the Besson–Dumais rule (8).

The proposed molecular mechanism behind the Besson–Dumais rule involves the perception of geometry-derived cues and their integration via the organization of cytoplasmic microtubules (8). Interestingly, ablation experiments and analog models suggest that cytoplasmic strands, populated with microtubules, are under tension (9, 10). These strands would guide the relocation of the nucleus at the cell center of mass before division and coalesce into the phragmosome at the future division site. Tension could reinforce selection of the shortest path (8). Consistently, the application of mechanical perturbations to plant tissues or cells can affect the next division plane orientation, although with sometimes contradictory results (11–13).

There is also indirect evidence that tension may play a role in division plane orientation: Before cell division, cortical microtubules reorganize in a ring called the preprophase band (PPB), which determines the position of the new cell wall (14). There is now accumulating evidence that cortical microtubules align along maximal tensile stress in cell walls, whether stress is subcellular or supracellular (15, 16). Therefore, cortical microtubules may serve as intermediates between tension patterns in cell walls and cell division plane orientation. In the most general scenario, such tensile stress may be prescribed not only by cell geometry but

Significance

The control of cell division plane orientation is crucial in biology and most particularly in plants, in which cells cannot rearrange their positions, as they are glued to each other by their cell walls. Cell geometry has long been proposed to determine cell division plane orientation. Here, using statistical analysis, modeling, and live imaging in the *Arabidopsis* shoot apex, we show that plant cells instead divide along maximal tension.

Author contributions: M.L., J.-D.J., A.B., and O.H. designed research; M.L., J.-D.J., and O.H. performed research; M.L., J.-D.J., and V.M. analyzed data; and M.L., J.-D.J., and O.H. wrote the paper.

The authors declare no conflict of interest.

This article is a PNAS Direct Submission.

Freely available online through the PNAS open access option.

[1]To whom correspondence may be addressed. Email: olivier.hamant@ens-lyon.fr or arezki.boudaoud@ens-lyon.fr.

This article contains supporting information online at www.pnas.org/lookup/suppl/doi:10.1073/pnas.1600677113/-/DCSupplemental.

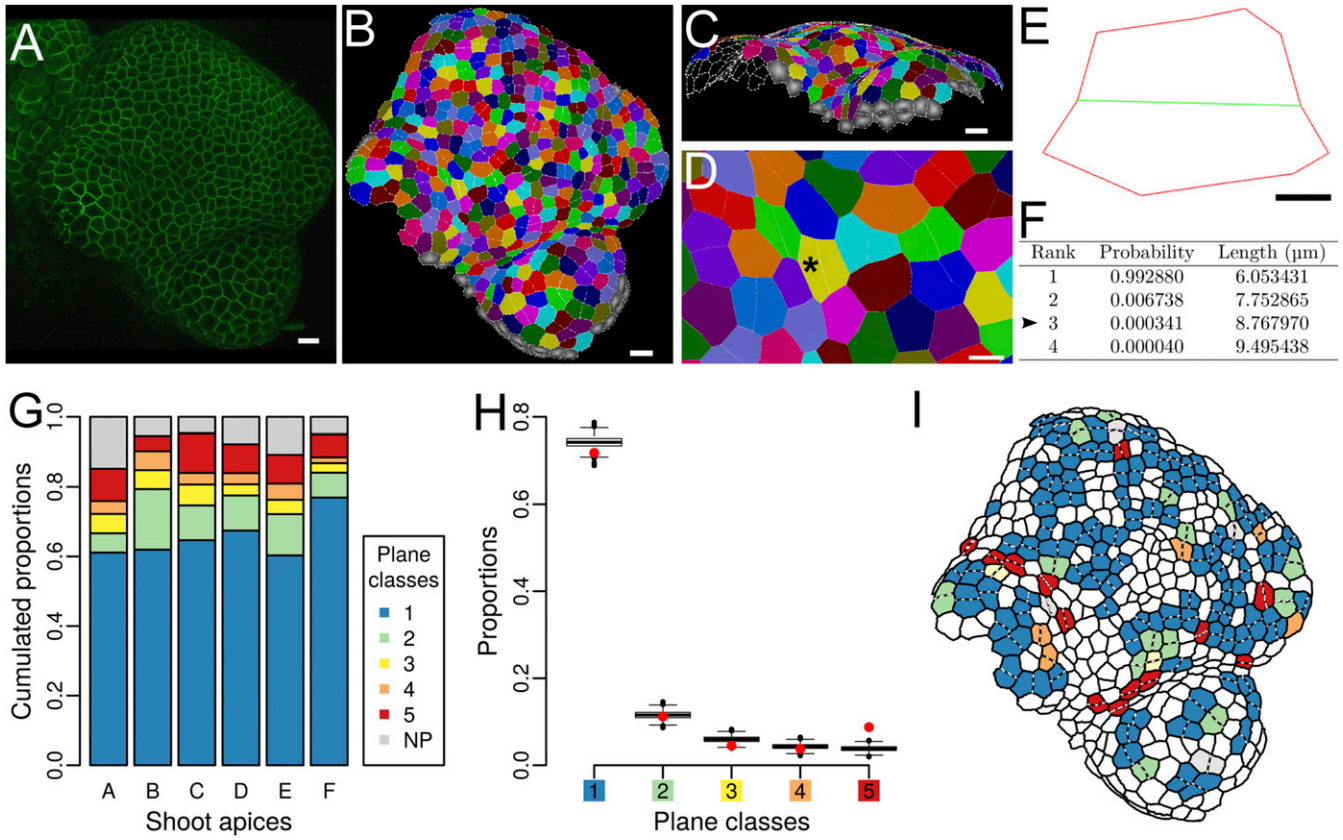

Fig. 1. Division planes at the shoot apex of *Arabidopsis thaliana*. (*A*) Confocal image of a *LTi6B-GFP* (WS-4) dissected shoot apex. (Scale bar, 10 μm.) (*B*) Cellular segmentation of the shoot apex shown in *A* with MorphoGraphX. Cells sharing the same color are daughters from a division that occurred during the last 12 h. (Scale bar, 10 μm.) (*C*) Segmentation is performed on the surface of the shoot apex. (Scale bar, 10 μm.) (*D*) Close-up of *B* on a young boundary region. The black asterisk points at a mother cell (i.e., two fused daughter cells), which is analyzed with Besson–Dumais script in *E* and *F*. (Scale bar, 5 μm.) (*E*) Flattened mother cell resulting from the 2D projection of vertices with a principal components analysis (PCA) (Fig. S2 *B* and *C*). Only the main vertices (i.e., at the junction between three cells) are kept as input for Besson–Dumais script. The new plane is colored in green. (Scale bar, 2 μm.) (*F*) First four planes predicted by the Besson–Dumais script for cell *E*. Arrowhead: The observed plane in cell *E* corresponds to the predicted plane of rank 3. The associated pairwise probability p_{pw} is equal to 3.4×10^{-4} and thus this cell belongs to the fifth plane class. (*G*) Proportion of the different plane classes in six shoot apices (total numbers of symmetrically dividing cells in the shoot apices A, B, C, D, E, and F are, respectively, 44, 71, 150, 218, 164, and 182). Class 1 corresponds to the choice of the shortest plane and class 5 corresponds to the choice of one of the longest planes. NP corresponds to an absence of match between theoretical predictions of the Besson–Dumais script and observations. (*H*) Comparison of observed plane proportions within the different classes (red circles) with fluctuation range obtained by bootstrap among theoretical predictions given by the Besson–Dumais script (boxplots). Planes that did not match any prediction (NP class) were excluded from this analysis. Total number of symmetrically dividing cells matching predictions on the six shoot apices (A, B, C, D, E, and F): 772. (*I*) Map of the shoot apex shown in *A* and segmented in *B* displaying plane classes for the divisions that occurred in the 12 h following this snapshot.

also by the behavior of adjacent cells. Altogether, this suggests that, rather than geometry *sensu stricto*, plant cells may sense tension to orient their division plane.

Because the Besson–Dumais rule has been tested only in tissues with rather local spherical shape or homogeneous growth, the relative roles of cell geometry and tension, and thus the contribution of adjacent cells, in division plane orientation remain to be shown. These roles are what we investigated here, using the whole shoot apex of *Arabidopsis thaliana*, which comprises not only the shoot apical meristem proper, but also the emerging primordia and the saddle-shaped boundary domain separating the meristem and the primordia. This larger tissue exhibits various levels of growth heterogeneity and curvature anisotropy, in which tension can be more or less anisotropic.

Results

Only Three of Four Cells Select the Shortest Division Plane in the Shoot Apex Epidermis. To test whether the Besson–Dumais rule can recapitulate all cell division plane orientations at the shoot apex, we computed the predictions of the Besson–Dumais rule for the divided cells on the epidermis of the shoot apex of *A. thaliana*. We first acquired confocal images of *LTi6B-GFP* (WS-4) dissected meristems every 12 h during 48 h (Fig. 1*A*). On each snapshot, the surface of the shoot apex was reconstructed and segmented with MorphoGraphX (17) to extract cell shapes (*Materials and Methods* and Fig. 1 *B–D*). Segmented mesh was cellularized with a minimal wall length of 1 μm to compute daughter cell areas and aspect ratios, and with a minimal wall length of 3 μm to extract cell contour as an input for the Besson–Dumais script (*Materials and Methods* and Fig. S1). New cell walls were identified by a visual comparison between snapshots (from $T = 12$ h to $T = 48$ h). We hypothesized that cell shape did not change much immediately after division and thus that the recorded cell wall position between the two daughter cells corresponded to the former PPB position in the mother cell.

Several conditions apply to the Besson–Dumais rule. First, it was implemented only for cell divisions recorded in a 2D plane. Because the shoot apex epidermis has an almost constant thickness of around 5 μm and new cell walls in this layer are perpendicular to the surface, i.e., anticlinal (Fig. S2*A* and figure S1 in ref. 18), we could restrict our analysis to the surface of the shoot apex. Although the curvature of the shoot apex surface can vary greatly (Fig. 1*C* and Fig. S2*A*), the surface of a pair of daughter cells is small enough to be locally flattened in 2D

without too much cell shape deformation (*Materials and Methods* and Fig. S2 *B–D*). Second, the Besson–Dumais rule applies only to symmetrically dividing cells. Comparison of the areas of the two daughter cells computed on the surface showed that 81% of the cells of the shoot apex divided almost equally, i.e., the smallest daughter cell occupying between 40% and 50% of the sum of the two daughters areas (Fig. S2*E*). The remaining 22% of asymmetrically dividing cells were located preferentially in the meristem region (Fig. S2*F*, and Fig. 2*A* for the definition of the shoot apex regions). In the following, these asymmetrically dividing cells were removed from the analysis.

We finally computed predictions of the Besson–Dumais rule, using the corresponding script (*Materials and Methods*). First, for each cell, the Besson–Dumais script seeks the shortest plane between each pair of edges that divides the mother's area (i.e., in our dataset, the area of the fused daughter cells) equally. Note that in a few cases, the Besson–Dumais script could not find any solution satisfying the condition on area for a given pair of edges. All possible planes were ranked from the shortest to the longest. The probability P_i to divide along a given plane i depends on the length of the plane (8) and takes the form:

$$P_i = \frac{e^{-\beta \ell_i/\rho}}{\sum_{j=1}^{N} e^{-\beta \ell_j/\rho}}, \quad [1]$$

where ℓ_i is the length of plane i, ρ is the mean cell diameter, β is a constant, and N is the total number of theoretical possible planes for this cell. Second, the Besson–Dumais script compares theoretical predictions to observations and provides the rank of the observed plane and its probability P_i to be chosen among all of the possibilities (Fig. 1*F* and Figs. S1 and S3). More precisely, the Besson–Dumais script compares each pair of edges connected to a predicted cell wall to the pair of edges connected to the observed cell wall. In 5–14% of the cases (depending on the shoot apex), the Besson–Dumais script did not find a match between theoretical predictions and observations. These observed planes are referred to as "not predicted" (NP) planes (by Besson–Dumais script), whereas others are referred to as "predicted."

As cells in the shoot apex display different geometries and as the number of possible planes may vary from one cell to another, ranks are not sufficient to compare cells with one another. As shown in Fig. S3, the shortest plane (rank = 1) in an elongated cell (Fig. S3*A*) has a higher probability P_1 to be observed than the shortest plane (rank = 1, also) of a roundish cell (Fig. S3*C*). To suppress this shape effect, we added a normalization step: We compared all predicted planes of a given cell with the shortest predicted plane of that cell. To do so, we computed the pairwise probability p_{pw} between the shortest predicted plane of length ℓ_1 (e.g., Errera's predicted plane) and the observed plane of length ℓ_{obs}, with $\ell_1 \leq \ell_{obs}$, as the ratio between the probability P_{obs} of the observed plane and the sum of the probabilities P_{obs} and P_1 (probability to observe the shortest plane):

$$p_{pw} = \frac{P_{obs}}{P_1 + P_{obs}}. \quad [2]$$

Pairwise probability p_{pw} varies between 0 (long plane) and 0.5 (short plane). When the observed plane is the shortest one (as, for instance, in Fig. S3*A*), pairwise probability is strictly equal to 0.5. We defined five classes of pairwise probability, =0.5, [0.375; 0.5[, [0.250; 0.375[, [0.125; 0.250[, [0; 0.125[, and added a sixth class when no match between theoretical predictions and observations could be found. These classes are later referred as plane classes. The first plane class corresponds to the choice of the shortest plane by the cell. Plane classes are not strictly equivalent to ranks, but they are independent of cell shape (Fig. S4).

Based on these analyses, we could observe that, between the different shoot apices, proportions of plane classes were similar but not identical (Fig. 1*G*). We found that, depending on the shoot apex, 65–77% of all planes (corresponding to 68–81% of predicted planes) corresponded to the shortest plane.

The Boundary Region Is Enriched in Long Planes. At the shoot apex, meristematic cell shapes are rather isodiametric (Fig. S5*A*), when compared to cell shapes in hypocotyls or roots. Thus, the length difference between the shortest and the second shortest plane is small and probabilities P_1 and P_2 are close. In theory, this could be sufficient to explain the relatively high proportion of cells avoiding the shortest plane at the shoot apex. To get the likelihood to obtain the proportions of plane classes we observed at the shoot apex, when cells follow the Besson–Dumais rule, we used a bootstrap approach. We sampled 1,000 sets of planes from the predictions of the Besson–Dumais script for dividing cells at the shoot apex and computed the corresponding plane class proportions. To obtain a given set of planes, for each dividing cell at the shoot apex that had chosen a plane predicted by the Besson–Dumais script, we sampled a new plane among the theoretical predictions given by the Besson–Dumais script. The probability to sample this plane i was equal to the probability P_i described above. We then computed the pairwise probability p_{pw} between the shortest predicted plane of length ℓ_1 and the sampled plane s of length ℓ_s, with $\ell_1 \leq \ell_s$. We obtained a first set of simulated pairwise probabilities and computed the proportions of each of the plane classes defined previously. We repeated this procedure 1,000 times to generate 1,000 sets of planes and the corresponding proportions for each plane class. We then plotted the boxplots of proportions for each plane class and added our observed proportions on the same graph (Fig. 1*H*). The boxplot (with its notches) represents a confidence interval at 95%. For a given plane class, if the observed proportion (red circles in Fig. 1*H*) is out of the boxplot, this means that the probability to get this proportion of planes, under the hypothesis that cells at the shoot apex follow the Besson–Dumais rule, is lower than 5%. Our analysis revealed that the probabilities to get the observed proportions of plane classes 1–4 are above 5%, whereas the probability to get the observed proportion of class 5 is below 5%. This result indicates that long planes are overrepresented and

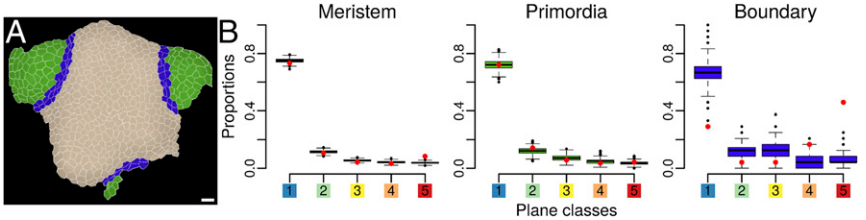

Fig. 2. A domain-based comparison between observations at the shoot apex and predictions of the Besson–Dumais rule. (*A*) Example of expert manual definition of the boundary domain (blue), the meristem domain (beige), and the primordia domains (green) on a shoot apex. (*B*) Comparison of observed plane proportions (red circles) with fluctuation range obtained by bootstrap among the theoretical predictions given by the Besson–Dumais script (boxplots), displayed in function of regions. Planes that were not predicted by the Besson–Dumais script (NP planes) were excluded from this analysis. Total numbers of symmetrically dividing cells in the meristem, primordium, and boundary regions, for which the observed plane was predicted by the Besson–Dumais script, are, respectively, 616, 133, and 23.

that the Besson–Dumais rule only partially accounts for observed planes at the shoot apex of *A. thaliana*.

Mapping of the divided cells colored in function of plane classes on the shoot apices indicated a nonrandom spatial distribution of plane classes (Fig. 1*I*). We thus spatialized the results of the bootstrap analysis to evaluate whether proportions of plane classes could be correlated to regional cues at the shoot apex. Three regions were defined manually: the meristem, including both the central zone and the peripheral zone (see, for instance, ref. 19 for a definition of these two zones); the outgrowing primordia; and the boundary, between the primordia and the meristem (Fig. 2*A*). The localization of each cell was determined based on the time point preceding cell division. In primordia, proportions of plane classes were found to be within the confidence interval, showing a good agreement between Besson–Dumais rule predictions and observed planes (Fig. 2*B*). In contrast, in the boundary, the probability to get the observed proportion of planes of classes 1, 4, and 5 was lower than 5% (Fig. 2*B*). In that region, the proportion of planes of class 1 was lower than predicted by our bootstrap approach and, conversely, the proportion of planes of classes 4 and 5 was higher. Finally, in the meristem, the proportion of long planes was slightly higher than expected. Note that this could be due to our restrictive definition of the boundary region. Therefore, although the Besson–Dumais rule correctly predicted the observed distribution of plane orientations in the meristem and primordia regions, it failed to predict the observed distribution of plane orientations in the boundary region.

A Mechanical Division Rule Provides Better Predictions for Division Plane Orientation at the Boundary. The boundary region can be distinguished from the primordia and the meristem regions by genetic factors, such as the expression of specific transcription factors (20, 21); by chemical factors, such as hormonal levels (e.g., refs. 22 and 23); or by geometrical factors, such as shape and growth. Meristem and primordia have a locally spherical shape and rather homogeneous growth, compared with the boundary, which exhibits a saddle shape and is characterized by a lower growth rate, compared with the surrounding tissues (24). The Besson–Dumais rule was validated on a wide variety of tissues coming from different species but with locally spherical shape (including flat organisms like *Coleochaete*, the corresponding sphere having a radius of infinite length) or homogeneous growth. Here we confirm that the Besson–Dumais rule applies to tissues with such properties, but we also find that it does not correctly predict the distribution of cell division plane orientation in tissues with anisotropic shape or differential growth, like the boundary domain at the shoot apex of *A. thaliana*.

Tissue shape may prescribe mechanical stress patterns. Under the hypothesis that the shoot apex behaves like a pressure vessel, with the epidermis acting as the main load-bearing layer, shape can affect stress patterns (25). The dome shape of the meristem and primordia prescribes isotropic stress patterns, whereas the saddle shape of the boundary region prescribes highly anisotropic tensile stresses along the crease axis (15) (see Fig. 6). Interphase cortical microtubules were shown to align with such tension at the boundary (15). An additional source of mechanical stress in this domain comes from differential growth, the boundary growing slower than the primordium. As differential growth and shape evolve concomitantly during boundary formation, separating the contribution of these two factors is complex. Simulations offer the possibility to simplify the system and test integrative hypotheses.

To compute the mechanics and the geometry of the tissue at the cellular scale, we used a vertex model. Our virtual tissue is a 2D lattice of growing and dividing cells. Roughly speaking, cells behave like rubber balloons, with a certain wall elasticity, under (turgor) pressure. They are packed together and thus cannot reach their rest shape. The discrepancy between the rest shape and the observed shape is a source of mechanical stress. Additional mechanical stress arises from supracellular patterns of differential growth (growth-derived stress) and/or from a supracellular tensile stress pattern imposed to the tissue, mimicking the stress prescribed by the curvature of the tissue (curvature-derived stress). Growth (e.g., displacement of vertices) is computed by minimizing the energy of the tissue, which is a balance between the elasticity of the cell walls resisting the tension imposed by the supracellular stress field and the pressure. Overall in the model, the stress in a given cell is a combination of the large-scale tissular stress and the small-scale stress driven by differences in growth rate. Cells divide when reaching a certain size threshold. In all of the simulations, the new division plane goes through the barycenter of the cell. Two division rules were tested: Either the new division plane follows the direction of the short axis of the cell (the geometrical division rule) or it follows the direction of local maximal tensile stress (the mechanical division rule). Combining the two rules and the two sources of supracellular stress, four cases of study were defined: growing tissue following either a geometrical or a mechanical division rule, undergoing either growth-derived or curvature-derived stress. To mimic the boundary region, the mechanical stress field is anisotropic. For growth-derived stress simulations, a ring of slow-growing cells surrounds a disk of fast-growing cells. To match actual measurements of growth at the *Arabidopsis* shoot apex, growth is three times higher in the central disk than in the surrounding ring. For curvature-derived stress simulations, tensile stress is three times higher along the x axis than along the y axis.

We applied the Besson–Dumais script to the output of simulated tissues to compute predictions of the Besson–Dumais rule and compare with observed division planes. As done for real tissues, we computed pairwise probabilities between the observed plane and the shorter predicted plane and subdivided this variable into the six classes defined previously (Fig. 3). Simulations produced a few highly elongated cells (Fig. S5*B*). As most of the aspect ratios of observed dividing cells at the shoot apex were above 0.5 (Fig. S5*A*), simulated dividing cells with an aspect ratio below 0.5 were discarded from the analysis (see below for a discussion on cell aspect ratio in the simulations). Tissues simulated with the geometrical rule, both in growth- and in curvature-derived stress fields, displayed a majority of short planes, as expected (Fig. 3). The implemented geometrical division rule mimics Errera's simplified shortest-path rule, but does not follow exactly the same conditions: division planes orient along the short axis of the cell, with a straight cell wall going through the barycenter of the cell, but without conditions on the equality of the daughter's area. This difference may explain the existence of planes in classes 2–5. Tissues simulated with the mechanical division rule displayed a higher proportion of long planes than tissues simulated with the geometrical rule and a higher proportion of NP planes (Fig. 3). Such a trend qualitatively matches what we observe in the boundary domain of the shoot apex (Fig. S6).

To test whether predictions from the mechanical division rule in simulations matched observed distributions in real meristems, we also applied the bootstrap approach described previously on tissues simulated with the mechanical division rule. In curvature-derived anisotropic stress fields, we observed a depletion in planes of class 1 and an enrichment in planes of class 5, with a probability lower than 5% to get these two proportions (Fig. 3), similar to what was observed in the boundary region of the shoot apex (Fig. 2*B*). In growth-derived anisotropic stress fields, we could observe the same bias toward classes 1 and 5 when isolating slow- from fast-growing cells (Fig. 3). Note that in these last simulations, this bias could also partially originate from a boundary effect of the simulations, as slow-growing cells were located at the periphery of the tissue.

To further test the predictive power of the mechanical division rule, we analyzed another output of the simulations: the cell aspect ratio, i.e., the ratio of short over long cell axis. The geometrical division rule produced cells with a rather isodiametric shape, whereas the mechanical division rule produced more elongated shapes (Fig. S5*B*). In that case, elongated cells were

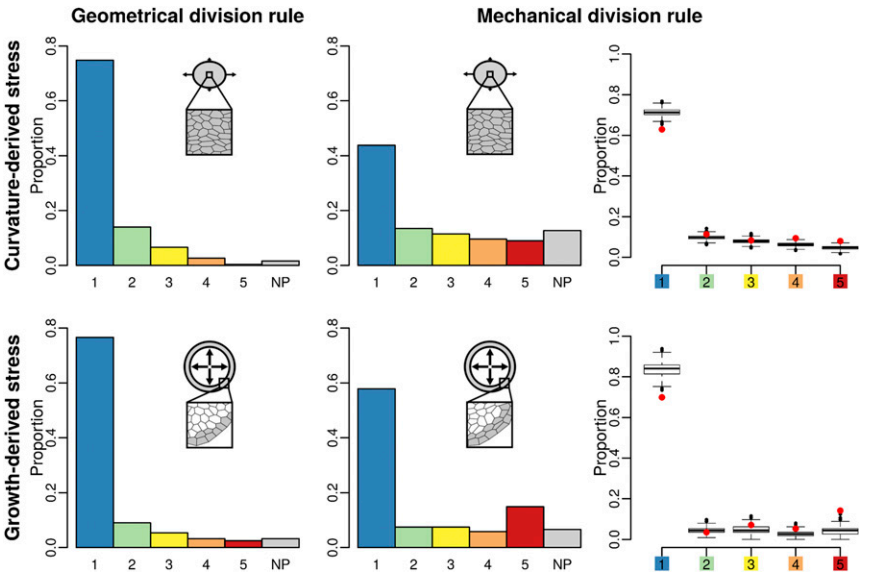

Fig. 3. Comparison of two division rules in a simulated boundary region. Shown are plane class proportions in the different simulated growing tissues, submitted either to curvature-derived or to growth-derived mechanical stress and following a geometrical or a mechanical division rule. For the simulations with the mechanical division rule, a bootstrap among theoretical predictions given by the Besson–Dumais script was done to compare observed plane proportions in simulated tissues (red circles) with fluctuations range (boxplots).

mostly located along maximal tensile stress in anisotropic curvature simulations and at the interface between the fast- and slow-growing tissues in the differential growth simulations. We then compared these quantifications to observations at the shoot apex. We measured a mean cell aspect ratio of 0.74 for the entire shoot apex. Boundary cells displayed a more anisotropic cell shape on average, with a mean aspect ratio of 0.58 (Fig. S5*A*). Thus, the mechanical division rule not only better predicts the distribution of plane classes in the boundary, but also produces tissues with a cell aspect ratio closer to that observed in boundary cells, where the stress field is anisotropic.

Mechanical Perturbations Impact Division Plane Orientation. If mechanical stress acts as a directional cue for division plane orientation, inducing an anisotropic mechanical stress pattern in an isotropic domain, like the meristem center, should also affect the cell division plane orientation. This is what we tested here.

Finite-element method (FEM) based simulations of a meristem epidermis under tension predict that an ablation induces circumferential maximal tensile stress directions in the cells adjacent to the ablated zone (15). First, we ensured that our vertex model also predicted such circumferential stress. On different simulated tissues undergoing homogeneous growth and isotropic external stress, a cell was removed from the template and the mechanical stress pattern before and after the ablation was analyzed (Fig. 4 *A* and *B*). As in FEM simulations, the mechanical stress pattern, which was random before ablation, became locally circumferential after the ablation (Fig. 4*B*).

We next performed single-cell ablations on real meristems with a pulsed UV laser (Fig. 4*C*) and computed the orientation of division planes in the neighboring cells 48 h after ablation (Fig. 4 *A*, *D*, and *E*). In the divided cells surrounding the ablation site, the new walls were oriented circumferentially around the wound, following the tensile stress pattern predicted by our simulations and FEM-based simulations (Fig. 4*F* and Fig. S7*A*). This experimental result thus supports an instructive role of tensile stress in division plane orientation at the shoot apex of *A. thaliana*. To further test this conclusion, we also performed double laser ablation on meristems, reasoning that this would prescribe a highly directional stress pattern in the cell surrounded by both ablations, as previously shown (15). To do so, we used the *clv3-2 GFP-MBD* background to have a larger central zone with isotropic stress before ablation. Not only did the cell divisions follow the stress pattern after ablation, but also a new cell wall could form at 90° from the former PPB (Fig. S7 *B*–*E*).

The meristem boundary exhibits strong anisotropic tensile stresses because of both differential growth and tissue curvature. One may thus question the generality of the mechanical rule, as this meristem region experiences such strong and directional stresses. To check this, we next designed a protocol in which the meristem is artificially flattened (Fig. S8*A* and *Materials and Methods*). We grew in vitro plants on 1-*N*-Naphthylphthalamic acid (NPA) to obtain a naked inflorescence, took the plants off NPA, and let the stem grow against a coverslip. In these conditions, organ initiation was triggered, albeit without any folding at the boundary; maximal tensile stress is thus prescribed only by differential growth between the organ and the meristem. As expected, cell division planes of many boundary cells followed the longest path, also parallel to maximal tension, matching the mechanical rule and opposing the geometrical rule (Fig. S8).

Conversely, if the mechanical rule is true, anisotropic tissue shape, in the absence of differential growth, may be sufficient to prescribe cell division plane orientation. To test this, we next observed the cell division plane in the inflorescence stems of young NPA-grown plants. As shown in previous studies, only the apical part of the inflorescence stem grows rapidly, as illustrated when using the microtubule depolymerizing drug oryzalin: The impact on growth is instead limited to the upper part of the stem (Fig. S9 *A* and *B*) (15, 26). This means that tensile stress in the bottom part of the stem is mainly prescribed by tissue shape and that these cells instead grow slowly. Because stems are roughly cylindrical, and assuming that the epidermis is under tension in that tissue, maximal tensile stress should be two times higher in the circumferential direction than in the axial direction (Fig. S9*A*). Consistently, we observed that most cell divisions in that region followed a circumferential direction, as predicted by the mechanical rule and not matching the Besson–Dumais rule (Fig. S9 *C*–*E*). Incidentally, these results confirm that the mechanical rule also applies to other tissues, beyond the shoot apex.

The Mechanical Division Rule Also Recapitulates Division Plane Orientations and Cell Aspect Ratios at the Meristem and Primordia. So far, we showed that a mechanical division rule better predicts division plane orientation than a geometrical division rule in the boundary domain where tensile stress is highly anisotropic. This, however, does not exclude the possibility that two rules may coexist in the shoot apex, a geometrical rule for isotropic domains and a mechanical rule for anisotropic domains.

Because the mechanical rule relies on the presence of tension in cell walls, it may in principle also be applied to tissues with locally spherical shape and homogeneous growth. In those

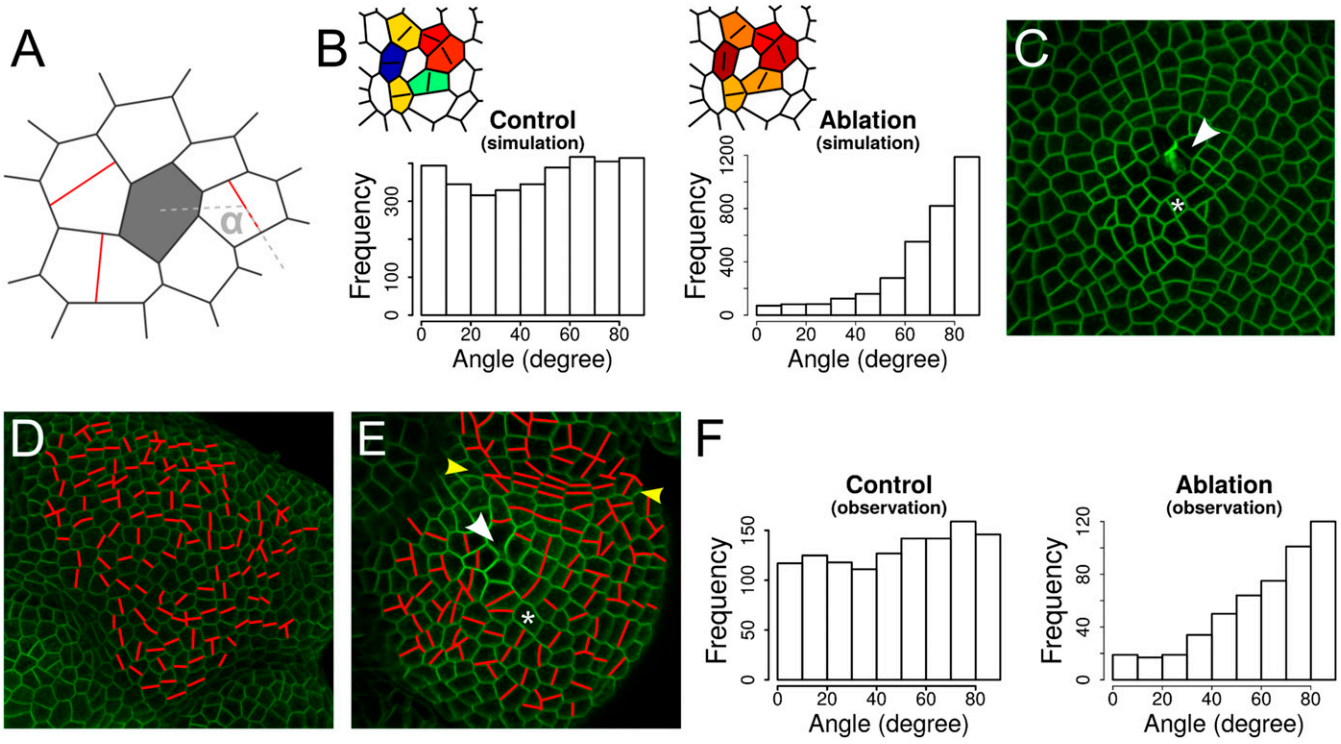

Fig. 4. Effects of mechanical perturbation on division plane orientation. (*A*) Angle α between the principal stress axis (simulated tissues) or the new cell wall (real tissues) and radius of the ablation. α is measured in each cell adjacent to the ablation site and on cells adjacent to these cells. (*B*) Angle α before and after ablation on simulated tissues. Close-up on a simulated tissue shows the direction of the maximal tension (black bars) within the cells neighboring an ablation site. Cells are colored according to the value of angle α, from blue (0°) to red (90°). (*C*) Confocal image of *LTi6B-GFP* (WS-4) dissected shoot apex 30 min after pulsed UV laser ablation. White arrowhead points at ablation site. White asterisk: same cell as in *E*. (*D* and *E*) New cell walls formed within 48 h (red lines) on (*D*) control and (*E*) ablated *LTi6B-GFP* (WS-4) dissected shoot apex. White arrowhead points at ablation site. Yellow arrowheads: boundary region. White asterisk: same cell as in *C*. (*F*) Distribution of the angle α in adjacent dividing cells of 36 ablated meristems. Control: 92 cells from three meristems are taken as "ablation site" and α is computed in the adjacent dividing cells (see Fig. S7 for a detailed analysis of the distribution of angle α in function of the location of ablation site on the meristem).

conditions, tensile stress within the cell wall would be derived only from cell geometry. As tension in the cell wall arises from the presence of turgor pressure inside the cell, the pressure vessel analogy can also be applied, this time on an individual cell (16). If a cell is elongated, then its top wall would be locally cylindrical, prescribing a circumferential stress pattern. This would promote the formation of transverse division planes in symmetrically dividing cells (see Fig. 6). In that situation, both mechanical and Besson–Dumais rules would provide similar predictions. The comparison between tensile stress maps and the cell short axis in our simulations supports this scenario (Fig. S10).

To test whether growth affects this conclusion, we simulated tissue growing in an isotropic stress field (same stress in x and y directions). In this case the mechanical stress in a cell is a combination of the global isotropic stress and the local mechanical stress induced by differences in growth rates between neighboring cells. We applied the Besson–Dumais script on the output of simulated tissues, and we computed classes of pairwise probabilities, as defined previously. We then applied the bootstrap approach described above on tissues simulated with the mechanical division rule to see how far this rule was from Besson–Dumais rule predictions in isotropic cases. The output of isotropic simulations (Fig. 5) was very similar to the Besson–Dumais predictions, thus suggesting that the mechanical division rule provides an equally satisfying prediction for cells dividing in isotropically growing tissues.

To further confirm this result, we also analyzed cell aspect ratios. We found that both curvature- and growth-derived stress fields produced tissues with similar cell aspect ratio, whether the division rule is geometrical or mechanical (Fig. S5*B*). Therefore, the mechanical division rule is also valid for tissues with isotropic curvature and/or homogeneous growth.

Discussion

Whereas Errera's rule and its generalization, the Besson–Dumais rule, correctly recapitulate cell division plane orientations in tissues with locally spherical shape and homogeneous growth, we showed here that they fail to account for cell division plane orientation when growth becomes heterogeneous and tissue curvature becomes anisotropic. In those situations, tissue stress is predicted to be anisotropic. Consequently, we propose instead that new cell walls orient along the local maximum of tensile stress in cell walls (Fig. 6). Importantly, tensile stress direction can be derived at a supracellular scale, tissue shape and differential growth prescribing regional anisotropic stresses. However, when the tissue is locally spherical and growth is homogeneous, tissue stress would be isotropic, and the only bias in tensile stress direction would be prescribed by cell shapes. In our simulations of 2D growing tissues, this mechanical division rule faithfully accounted for division plane orientations in regions with anisotropic stress as well as in regions with isotropic stress. Experimental perturbation of mechanical stress pattern and analysis of cell division planes in inflorescence stems further supported the contribution of mechanical stress as a directional cue orienting the cell division plane.

Because tensile stress can be prescribed by cell geometry and tissue behavior, this work echoes the analysis of microtubule behavior, and its relation to tension, in pavement cells: When the tissue is locally flat, cell geometry prescribes tensile stress, and thus cortical microtubule orientation, notably in the neck region of pavement cells, where they are well aligned along predicted

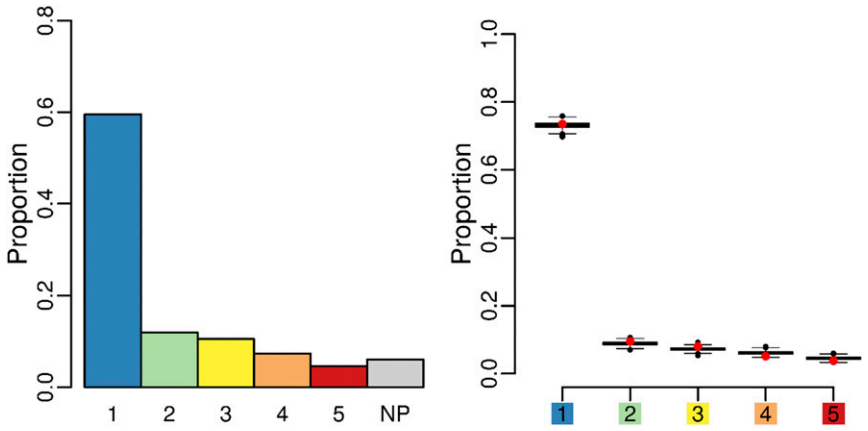

Fig. 5. Plane class proportions and bootstrap on simulated tissues growing in an isotropic stress field and following the mechanical division rule. Plane class proportions (barplot) and bootstrap among theoretical predictions given by the Besson–Dumais script were done to compare observed plane proportions in simulated tissues (red circles) with fluctuation range (boxplots).

maximal tension. However, the presence of a local hill (often associated with a stomata) in the tissue prescribes a circumferential tissue stress pattern matching circumferential microtubule orientations, largely independent of cell geometry (16).

Incidentally, our definition of the mechanical rule is deterministic (maximum of tensile stress), even though it is now well established that plant cell division includes an element of stochasticity (5, 6). Within the mechanical rule framework, stochasticity may still emerge from three factors: the time when the cell division plane orientation is assigned by stress [e.g., microtubule reorientation in response to stress may be fast or slow depending on the presence of regulators (18)]; the presence of other signals like auxin, which may oppose tensile stress prescriptions (e.g., ref. 27); and the threshold in intensity between stresses that are derived from cell geometry or tissue behavior (e.g., ref. 16).

Whereas research in cell biology is still largely based on single-cell approaches and focused on subcellular factors, there is an increasing interest in studying the contribution of adjacent cells to explain intracellular dynamics. For instance, the impact of the growth of adjacent cells on cell geometries was investigated in *C. orbicularis* (6). Note that in this tissue, Errera's rule, with noise, can still explain cell division plane orientation. Similarly the contributions of tissue topology and packing constraints have also been involved in cell division plane orientation, as division plane orientation was shown to be biased by the position of the surrounding cells' long axis in both animal and plant epithelia (28). However, these models invoke only the passive mechanical deformation of cells and thus support a cell geometry sensing mechanism. Our results confirm that differential growth or stress anisotropy can impact the cell geometry, and in particular the cell aspect ratio, as cells are more elongated when tissues grow in an anisotropic stress field. However, the geometrical rule is not sufficient to explain the overrepresentation of cell divisions along the longitudinal axis of the cell in the boundary region of the shoot apical meristem. Thus, the mechanical division rule we propose must involve an active perception of mechanical stress. As a consequence, if growth- or shape-derived stress becomes stronger or more directional than cell geometry-derived stress, the new cell division plane will be built to resist maximal tension, irrespective of cell geometry. To some extent, this rule brings together the cell and organismal theory of development by putting a multiscale cue forward. It also recalls Wolff's law (29, 30), which states that bones reinforce their internal structure by remodeling trabeculae according to maximal stress directions: A plant cell builds a new cell wall in the direction of maximal tension to resist it.

The presence of hormone gradients may also be invoked to explain why cells in the boundary would divide along the longest plane. Interestingly, auxin signaling is required to generate longer planes in *Arabidopsis* embryos (27). Auxin is largely depleted in the boundary domain of the SAM in a PIN1-dependent way (22, 31, 32). However, cells divide along one of the longest planes in that domain. The situation in the SAM might be more complex, and a contribution of auxin gradients in division plane orientations cannot be formally excluded. It is in fact very likely that both processes act synergistically to provide such reproducible outputs.

The molecular mechanism behind tension perception before cell division is still unclear. Microtubules in cytoplasmic strands are under tension (9) and interphasic cortical microtubules align with maximal tension (15). The physical interaction between cortical microtubules and cytoplasmic microtubules can be inferred from the close vicinity of the two networks, but has not been formally studied experimentally. In root cells of the male fern *Dryopteris filix-mas* where the nucleus is close to the plasma membrane, electron microscopy images suggest that cytoplasmic microtubules connected to the nucleus could bend when reaching the cortex and be intermingled with PPB microtubules (33). Based on these observations, but without further experimental proof, microtubules populating cytoplasmic strands were also proposed to bend and interact with PPB microtubules (34). Light-transmitted microscopic observations of vacuolated cells also attested to the close vicinity of the two microtubule networks at the cortex (9). The analysis of the molecular regulators of PPB formation will certainly offer some key insights into this process in the future (35, 36). Note that PPB formation is not omnipresent in plants, as microspores and endosperm in angiosperms, obliquely dividing cells in *Physcomitrella*, and *Arabidopsis* cells in culture do not form PPBs. This may suggest that one of the functions of the PPB is to coordinate cell division with supracellular cues, including tissue stress.

The molecular regulators of phragmoplast positioning may also be involved. In particular, myosin VIII was recently shown to associate with the edge of phragmoplast microtubules and, together with actin, to guide phragmoplast expansion to the cortical division site (37). Actin and myosin have also been recently involved in posture control, a process that heavily relies on the perception of mechanical cues (38), and actin also reorients circumferentially around ablations, like microtubules (39). Interestingly, spindle orientation in animal cells also depends on actin and tension (e.g., ref. 40), thus suggesting that some aspects of the molecular regulation of cell division by stress may be conserved across kingdoms too.

Materials and Methods

Plant Material and Growth Conditions. The *GFP-MBD* line (WS-4) was previously described in refs. 15 and 41 (MBD: microtubule binding domain). The *LTI6b-GFP* line (WS-4) was previously described in refs. 15 and 42 (LTI: low temperature induced). The *clv3-2 GFP-MBD* line (Ler/WS-4) was previously described in ref. 43 (clv3: clavata 3). The *LTI6b-GFP* line was sown on soil, kept at 4 °C for 48 h, and then grown in short-day conditions (8 h light at 19 °C, 16 h dark at 17 °C) for 4 wk and transferred to 2–3 wk in long-day conditions (16 h light at 21 °C , 8 h dark at 19 °C) before dissection.

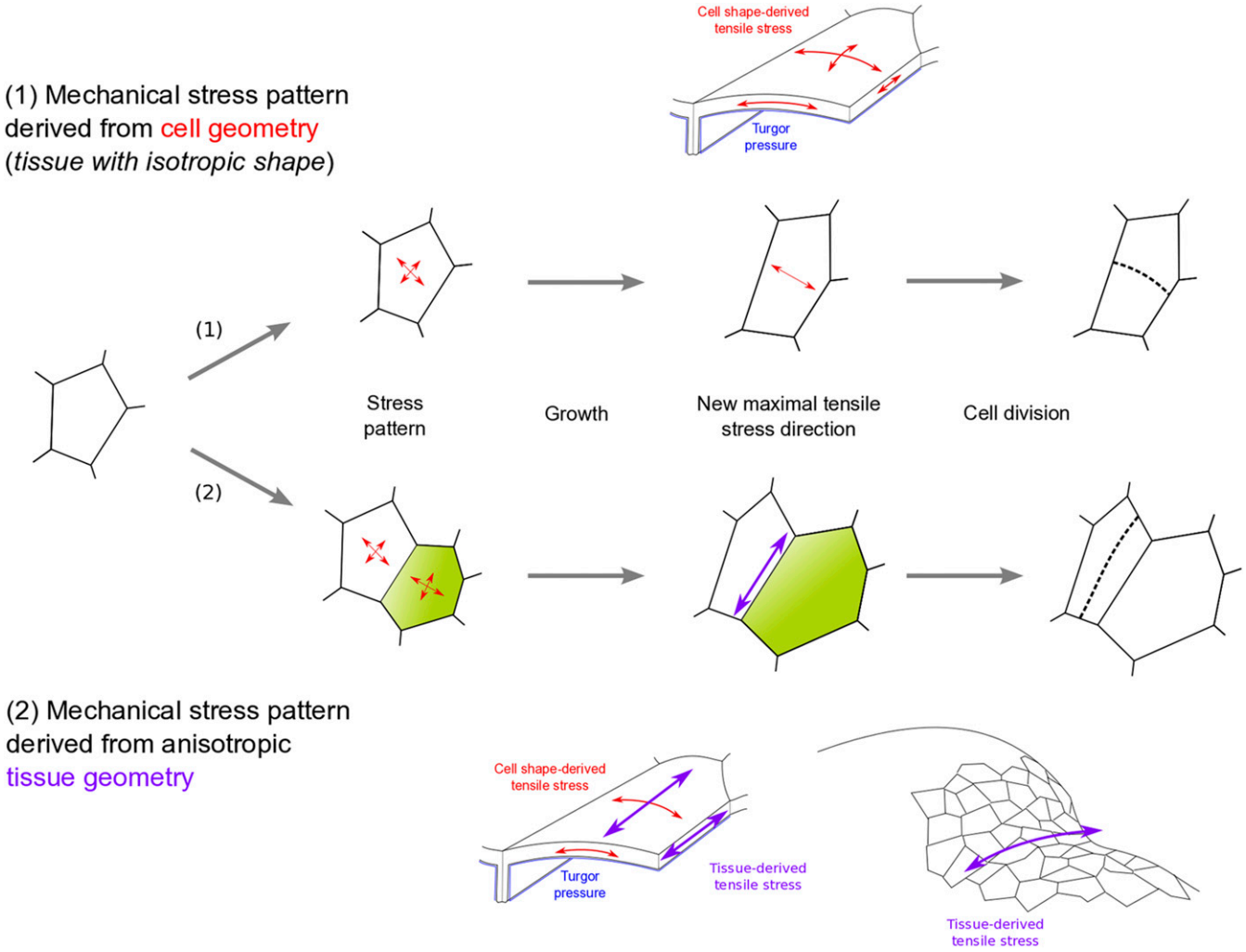

Fig. 6. Tensile stress prescribes cell division plane orientation in symmetrically dividing cells. (*Upper*) When growth is locally homogeneous and shape locally spherical, the tensile stress pattern in cell walls can be derived from cell geometry only, assuming that plant cells behave like pressure vessels. In that case, maximal tension will be circumferential in elongated, cylindrical cells, leading to transverse division plane orientation, as in Errera's rule. (*Lower*) When growth becomes heterogeneous and/or tissue shape is anisotropic, tensile stress in cell walls may be biased by tissue stress. For instance, in the meristem boundary, tissue curvature and differential growth prescribe highly anisotropic tensile stresses and cells divide along the axis of the boundary, relatively independent of cell shape.

Meristems were cut from the stem, dissected on the day before imaging, and stuck in "*Arabidopsis* apex culture medium" (2.2 $g{\cdot}L^{-1}$ Duchefa Biochemie MS basal salt mixture without vitamins, 1% sucrose, 0.8% agarose, pH 5.8), as described in ref. 44. Medium was supplemented with vitamins (0.1g/L myo-inositol; Sigma), nicotinic acid (1 mg/L; Sigma), pyridoxine hydrochloride (1 mg/L; Sigma), thiamine hydrochloride (10 mg/L; Sigma), glycine (2 mg/L; Sigma), and 6-benzylaminopurine (BAP) (555 $\mu mol{\cdot}L^{-1}$ for apices A and B and 200 $\mu mol{\cdot}L^{-1}$ for apices C–F on Fig. 1*G*). Dissected meristems were kept in a phytotron in long-day conditions (Sanyo; 16 h light at 20 °C, 8 h dark at 20 °C, synchronized with growth culture chambers).

Imaging. Stacks of 1,024 × 1,024 pixels of three dissected meristems, with Z slices every 0.5 μm, were acquired every 12 h during 48 h on a Zeiss LSM 700 upright confocal microscope, with a 40× water-dipping lens. Stacks from the kinetics were processed with a C++ script, using the Level Set method (45) to detect the surface of the meristem at high resolution. Meshes of these surfaces were then created with MorphoGraphX (17, 46). Surface geometry of the processed stack was extracted with a marching cube algorithm. The initial mesh had a 5-μm resolution. The mesh was smoothed and subdivided until its resolution went below membrane signal thickness (around 0.5 μm). Fluorescence signal (0–3 μm below the surface) was projected onto this mesh. Semiautomatic segmentation was performed using the watershed method, allowing delineation of cells. The mesh was cellularized with a minimal wall length of either 1 μm or 3 μm.

For each cell, lineage and localization (referred as "primordia," "boundary," and "meristem," e.g., central zone plus peripheral zone) were recorded manually for each 12-h snapshot. A boundary is defined as a curved region between an outgrowing primordium and the meristem. Because our definition of the boundary is rather strict, very young boundaries and primordia belong to the meristem region. Maps of area and curvature (with a radius of 20 μm) for each snapshot and growth rates and growth directions between each pair of contiguous snapshots were computed with MorphoGraphX. Each snapshot was exported as a .vtk text file, recording vertices coordinates and associations of vertices to cells. Lineage, localization of cells, growth, curvature, and area raw data were saved as separate text files. .vtk and other MorphoGraphX output text files were processed with R (47) to extract various cell indicators (orientation and length of long and short axis, area, growth rate, local direction, and intensity of curvature). For each of the snapshots between $T = 12$ h and $T = 48$ h, fused daughter cells that came from a division between previous and current snapshots were projected in 2D, using a principal component analysis on vertices. Principal component analyses were performed with the R package FactoMineR (48). Vertices were more spread in *x* and *y*, meaning that the third dimension always corresponded to *z*. The third dimension explained only a few percent of dispersion of vertices (between 0% and 2.5%, with a mean at 0.15% for all cells at the shoot apex and a slightly higher mean and variance when considering cells located in the boundary regions only, Fig. S2*D*), indicating that local flattening did not deform too much the mother cell shape. The first two

dimensions only were kept and vertices were ordered either clockwise or counterclockwise. Predictions given by the rule of Besson and Dumais were obtained with the Matlab (49) script written by Sébastien Besson (https://github.com/sbesson/plant-tissue). This script seeks the shortest plane between each pair of edges dividing the cell into two equal areas and ranks these planes according to their length. It then compares the observed plane with theoretical predictions and gives the rank of the plane and the probability to observe this plane.

Ablations. UV laser ablations were performed on an inverted Leica DMI4000 microscope, equipped with a confocal spinning disk head (Yokogawa CSU22), with a 20× dry lens. Imaging postablation was performed on a Zeiss LSM 700 upright confocal microscope, with a 40× water-dipping lens. Stacks were processed with MerryProj (50) to obtain a top-view 2D projection of the meristems. Localization from the ablation or the control site (i.e., "rank") was determined as follows: The center of the meristem was determined by approximating its shape to a circle touching the primordia, and concentric adjacent cell circles were drawn around this central point. New cell walls in neighbors adjacent to the ablation and adjacent to these neighbors were identified manually, using the layers and paths tool of the GNU Image Manipulation Program (51). Angles between the new plane and the radius of the ablation zone were measured with the Fiji angle tool (52).

Meristem Flattening. Naked inflorescences were obtained by growing young seedlings in vitro on NPA as previously described in ref. 15. When stems were long enough, the whole plantlet was placed in a box in which the stem was held with two blades (15). An adhesive silicone (MED-1356; NuSil Silicone Technology) was then applied onto a coverslip and rinsed once in water. The coverslip was then applied on top of the apex. Stem growth pushed the apex against the coverslip, flattening the apex for a period of 12–36 h. The apex was imaged as described above.

Inflorescence Stem Imaging and Oryzalin Treatment. Naked inflorescences were obtained by growing young seedlings in vitro on NPA as previously described in ref. 15. Stems were then embedded in 0.5% agarose between a slide and a coverslip to allow side-view imaging, using the protocol described above. For oryzalin treatment, agarose was removed and the whole plants were then immersed in a solution of 20 $\mu g \cdot L^{-1}$ oryzalin for 3 h, as described in ref. 15. Five days later, stems were embedded again in agarose and imaged.

Model. We modeled two possible mechanisms driving the positioning of the new wall during a cell division: The new wall can be positioned either to minimize its length or in the direction of highest tension. Then we compared the development of tissues following one or the other mechanism.

We used a vertex model that allows us to compute the mechanics and the geometry of the tissue at the same scale. The model is 2D but 3D information can be incorporated as an external stress.

Mechanics. The cells form a flat polygonal tilling, each polygon being a cell. The mechanics of a single cell C are driven by its anisotropic deformation $M_C - M_C^{(0)}$, where M_C is the actual shape of the cell and $M_C^{(0)}$ its equilibrium state. The shape tensor is computed as the covariance matrix

$$M_C = \frac{1}{N_C}\begin{pmatrix} \sum_{i=1}^{N_C}(x_i - x_C)^2 & \sum_{i=1}^{N_C}(x_i - x_C)(y_i - y_C) \\ \sum_{i=1}^{N_C}(x_i - x_C)(y_i - y_C) & \sum_{i=1}^{N_C}(y_i - y_C)^2 \end{pmatrix},$$

where (x_i, y_i) are the coordinates of the cell's vertices, (x_C, y_C) is the barycenter of the vertices, and N_C is the number of vertices. Thus, we are able to measure the anisotropy of the cells.

The position of the vertices is given by the minimization of the mechanical energy of the tissue. Taking into account the elasticity and the turgor pressure, we can define the energy of a single cell as

$$E_C = -pA_C + \frac{\alpha}{2}A_C\frac{\|M_C - M_C^0\|_F^2}{\mathrm{tr}^2(M_C^0)},$$

with p the pressure and α the shear modulus of the periclinal wall. The stress tensor of the periclinal wall is then given by the functional derivative of its energy density with respect to its strain:

$$S_C = \frac{\partial\left(\alpha\frac{\|M_C - M_C^0\|_F^2}{\mathrm{tr}^2(M_C^0)}\right)}{\partial\left(\frac{M_C - M_C^0}{\mathrm{tr}(M_C^0)}\right)} = \alpha\frac{M_C - M_C^0}{\mathrm{tr}(M_C^0)}.$$

In a folded boundary, stress is predicted to be anisotropic. Therefore, to take into account the curvature of a real tissue, an external stress is introduced into the energy of the whole tissue,

$$E_T = \sum_C E_C - A_T\frac{M_T - M_T^0}{\mathrm{tr}(M_T^0)} : S_T,$$

where A_T is the area of the tissue, M_T is its shape, M_T^0 is its reference shape, and S_T is the external stress. The reference shape of the tissue is computed by minimizing the energy without the external term.

As new divisions in the epidermis of the shoot apical meristem are anticlinal (see Fig. S2*A*), we hypothesized that mechanical stress within periclinal cell walls controls the orientation of new anticlinal cell walls. Thus, we simulated only mechanics of periclinal cell walls.

Tissue Growth. Because of the turgor pressure and the cellular interactions, the cells' shapes are different from their targets when the mechanical energy is minimal. To model the growth as the evolution of the equilibrium state of the cell, the target matrix evolves proportionally to its difference from the actual shape,

$$\frac{dM_C^0}{dt} = a_C(M_C - M_C^0),$$

where a_C is the remodeling rate of the cell.

We used an incremental approach to growth: After minimizing the mechanical energy, the targets evolve according to the differential equation system.

Cell Division. During cell growth, if the area of a cell is greater than the division threshold, the cell is divided according to one of the two following rules.

For the geometrical hypothesis, we mimicked the simplified shortest path version of Errera's rule (4) by choosing the division direction $\vec{n}$ as the one that minimizes the shape of the cell:

$$\vec{n},\ \vec{n}^t M_C \vec{n} = \min\left\{\vec{u}^t M_C \vec{u}\right\}_{\|\vec{u}\|=1}.$$

For the mechanical hypothesis, the division direction $\vec{n}$ is the one that maximizes the stress:

$$\vec{n},\ \vec{n}^t S_C \vec{n} = \max\left\{\vec{u}^t S_C \vec{u}\right\}_{\|\vec{u}\|=1}.$$

The cell is divided by a straight line going through its center, which is defined as the barycenter of its vertices.

Properties of the Daughter Cells. After division, the growth rate of the daughter cells is equated with the growth rate of the mother cell:

$$a_D = a_M.$$

The targets of the daughter cells are chosen to keep the stress constant over the division,

$$\frac{M_D - M_D^0}{\mathrm{tr}(M_D^0)} = \frac{M_M - M_M^0}{\mathrm{tr}(M_M^0)},$$

where D stands for a daughter cell and M for the mother cell. One can show that this relation is equivalent to the following definition for the daughter's target:

$$M_D^0 = M_D + \frac{\mathrm{tr}(M_D)}{\mathrm{tr}(M_M)}(M_M^0 - M_M).$$

As the two neighboring cells in the direction of the division get a new vertex, their shape matrix is slightly modified. Therefore, their targets are also adapted to keep the mechanical stress constant. The relation is identical,

$$M^0_{C'} = M_{C'} + \frac{\mathrm{tr}(M_{C'})}{\mathrm{tr}(M_C)}\left(M^0_C - M_C\right),$$

where C and C' stand for the neighboring cell before and after the division.

Implementation. The model was implemented in a C program. The energy was minimized using the BFGS algorithm (53), implemented in the NLopt library (54). The differential equation system was solved using the GNU Scientific Library (55). Outputs were analyzed with Scilab (56). Simulation parameters were $p = 0.01$ for the turgor pressure, $\alpha = 2$ for the shear modulus, $S_{T,xx} = 0.03$ and $S_{T,yy} \in \{0.01, 0.03\}$ for the curvature-derived stress, and $a_C \in \{0.3, 1\}$ for the growth rate. Initially the energy was minimized every $\Delta t = 10^{-2}$, but this time step was reduced proportionally to the number of cells to keep a constant temporal resolution on the divisions. Mechanical parameters were set to lead to a strain corresponding to a few percent, as is observed in real tissues. The external stress was estimated to vary between 1 and 10 times the pressure stress; thus we set the parameters so that the external stress contribution is 75% of the total stress. The tissues are initially 100 cells in volume and grow up to 200 cells. Noise in the initial conditions and in the growth rates allows us to perform each kind of simulation several times. The noise in the initial conditions is a random displacement of each vertex whose maximal amplitude is as large as possible without any vertex crossing a cell wall. The noise in the growth rates was a white noise of amplitude 10% that was reset at each time step.

ACKNOWLEDGMENTS. We thank Sébastien Besson and Jacques Dumais for providing guidance to M.L. in the initial steps of this work. We thank Jan Traas for his support. We also thank Platim (UMS 3444 Biosciences Gerland–Lyon Sud) for help with imaging and Centre Blaise Pascal (ENS de Lyon) for information technology support. This work was supported by a PhD grant from ARC3 Environnement, Région Rhône-Alpes, and by the European Research Council Grants 615739 "MechanoDevo" and 307387 "PhyMorph."

1. Sahlin P, Jönsson H (2010) A modeling study on how cell division affects properties of epithelial tissues under isotropic growth. *PLoS One* 5(7):e11750.
2. Hofmeister W (1863) Zusatze und berichtigungen zu den 1851 veröffentlichen untersuchungen der entwicklung höherer kryptogamen. *Jahrbucher fur Wissenschaft und Botanik* 3:259–293. German.
3. Sachs J (1878) Uber die Anordnung der Zellen in jungsten Pflanzentheilen. *Arbeiten des Botanisches Institut Wurzburg* 2:46–104. German.
4. Errera L (1888) Über Zellformen und Seifenblasen. *Botanisches Centralblatt* 34: 395–398. German.
5. Besson S, Dumais J (2014) Stochasticity in the symmetric division of plant cells: When the exceptions are the rule. *Front Plant Sci* 5:538.
6. Dupuy L, Mackenzie J, Haseloff J (2010) Coordination of plant cell division and expansion in a simple morphogenetic system. *Proc Natl Acad Sci USA* 107(6):2711–2716.
7. Shapiro BE, Tobin C, Mjolsness E, Meyerowitz EM (2015) Analysis of cell division patterns in the *Arabidopsis* shoot apical meristem. *Proc Natl Acad Sci USA* 112(15): 4815–4820.
8. Besson S, Dumais J (2011) Universal rule for the symmetric division of plant cells. *Proc Natl Acad Sci USA* 108(15):6294–6299.
9. Flanders DJ, Rawlins DJ, Shaw PJ, Lloyd CW (1990) Nucleus-associated microtubules help determine the division plane of plant epidermal cells: Avoidance of four-way junctions and the role of cell geometry. *J Cell Biol* 110(4):1111–1122.
10. Goodbody KC, Venverloo CJ, Lloyd CW (1991) Laser microsurgery demonstrates that cytoplasmic strands anchoring the nucleus across the vacuole of premitotic plant cells are under tension. Implications for division plane alignment. *Development* 113: 931–939.
11. Lintilhac PM, Vesecky TB (1981) Mechanical stress and cell wall orientation in plants. II. The application of controlled directional stress to growing plants; with a discussion on the nature of the wound reaction. *Am J Bot* 68(9):1222–1230.
12. Lintilhac PM, Vesecky TB (1984) Stress-induced alignment of division plane in plant tissues grown in vitro. *Nature* 307:363–364.
13. Lynch TM, Lintilhac PM (1997) Mechanical signals in plant development: A new method for single cell studies. *Dev Biol* 181(2):246–256.
14. Rasmussen CG, Wright AJ, Müller S (2013) The role of the cytoskeleton and associated proteins in determination of the plant cell division plane. *Plant J* 75(2):258–269.
15. Hamant O, et al. (2008) Developmental patterning by mechanical signals in Arabidopsis. *Science* 322(5908):1650–1655.
16. Sampathkumar A, et al. (2014) Subcellular and supracellular mechanical stress prescribes cytoskeleton behavior in Arabidopsis cotyledon pavement cells. *eLife* 3:e01967.
17. Barbier de Reuille P, et al. (2015) MorphoGraphX: A platform for quantifying morphogenesis in 4D. *eLife* 4:05864.
18. Uyttewaal M, et al. (2012) Mechanical stress acts via katanin to amplify differences in growth rate between adjacent cells in Arabidopsis. *Cell* 149(2):439–451.
19. Laufs P, Grandjean O, Jonak C, Kiêu K, Traas J (1998) Cellular parameters of the shoot apical meristem in Arabidopsis. *Plant Cell* 10(8):1375–1390.
20. Aida M, Tasaka M (2006) Genetic control of shoot organ boundaries. *Curr Opin Plant Biol* 9(1):72–77.
21. Rast MI, Simon R (2008) The meristem-to-organ boundary: More than an extremity of anything. *Curr Opin Genet Dev* 18(4):287–294.
22. Heisler MG, et al. (2005) Patterns of auxin transport and gene expression during primordium development revealed by live imaging of the Arabidopsis inflorescence meristem. *Curr Biol* 15(21):1899–1911.
23. Brunoud G, et al. (2012) A novel sensor to map auxin response and distribution at high spatio-temporal resolution. *Nature* 482(7383):103–106.
24. Kwiatkowska D, Dumais J (2003) Growth and morphogenesis at the vegetative shoot apex of Anagallis arvensis L. *J Exp Bot* 54(387):1585–1595.
25. Boudaoud A (2010) An introduction to the mechanics of morphogenesis for plant biologists. *Trends Plant Sci* 15(6):353–360.
26. Sassi M, et al. (2014) An auxin-mediated shift toward growth isotropy promotes organ formation at the shoot meristem in Arabidopsis. *Curr Biol* 24(19):2335–2342.
27. Yoshida S, et al. (2014) Genetic control of plant development by overriding a geometric division rule. *Dev Cell* 29(1):75–87.
28. Gibson WT, et al. (2011) Control of the mitotic cleavage plane by local epithelial topology. *Cell* 144(3):427–438.
29. D'Arcy Thompson W (1917) *On Growth and Form* (Cambridge Univ Press, Cambridge, UK).
30. Wolff J (1892) *Das Gesetz der Transformation der Knochen*; trans Maquet P, Furlong R (1986) [*The Law of Bone Remodeling*] (Springer, Berlin). German.
31. Reinhardt D, et al. (2003) Regulation of phyllotaxis by polar auxin transport. *Nature* 426(6964):255–260.
32. de Reuille PB, et al. (2006) Computer simulations reveal properties of the cell-cell signaling network at the shoot apex in Arabidopsis. *Proc Natl Acad Sci USA* 103(5): 1627–1632.
33. Burgess J (1970) Interactions between microtubules and the nuclear envelope during mitosis in a fern. *Protoplasma* 71(1–2):77–89.
34. Bakhuizen R, Van Spronsen PC, Sluiman-den Hertog FAJ, Venverloo CJ, Goosen-de Roo L (1985) Nuclear envelope radiating microtubules in plant cells during interphase mitosis transition. *Protoplasma* 128(1):43–51.
35. Drevensek S, et al. (2012) The Arabidopsis TRM1-TON1 interaction reveals a recruitment network common to plant cortical microtubule arrays and eukaryotic centrosomes. *Plant Cell* 24(1):178–191.
36. Spinner L, et al. (2013) A protein phosphatase 2A complex spatially controls plant cell division. *Nat Commun* 4:1863.
37. Wu SZ, Bezanilla M (2014) Myosin VIII associates with microtubule ends and together with actin plays a role in guiding plant cell division. *eLife* 3:e03498.
38. Okamoto K, et al. (2015) Regulation of organ straightening and plant posture by an actin–myosin XI cytoskeleton. *Nature Plants* 1(4):15031.
39. Goodbody KC, Lloyd CW (1990) Actin filaments line up across Tradescantia epidermal cells, anticipating wound-induced division planes. *Protoplasma* 157(1):92–101.
40. Théry M, Bornens M (2006) Cell shape and cell division. *Curr Opin Cell Biol* 18(6): 648–657.
41. Marc J, et al. (1998) A GFP-MAP4 reporter gene for visualizing cortical microtubule rearrangements in living epidermal cells. *Plant Cell* 10(11):1927–1940.
42. Cutler SR, Ehrhardt DW, Griffitts JS, Somerville CR (2000) Random GFP:cDNA fusions enable visualization of subcellular structures in cells of *Arabidopsis* at a high frequency. *Proc Natl Acad Sci USA* 97(7):3718–3723.
43. Heisler MG, et al. (2010) Alignment between PIN1 polarity and microtubule orientation in the shoot apical meristem reveals a tight coupling between morphogenesis and auxin transport. *PLoS Biol* 8(10):e1000516.
44. Hamant O, Das P, Burian A (2014) Time-lapse imaging of developing meristems using confocal laser scanning microscope. *Plant Cell Morphogenesis*, eds Žárský V, Cvrčková F (Humana Press, Totowa, NJ), Vol 1080, pp 111–119.
45. Landrein B, et al. (2015) Mechanical stress contributes to the expression of the STM homeobox gene in Arabidopsis shoot meristems. *eLife* 4:e07811.
46. Kierzkowski D, et al. (2012) Elastic domains regulate growth and organogenesis in the plant shoot apical meristem. *Science* 335(6072):1096–1099.
47. R Core Team (2015) *R: A Language and Environment for Statistical Computing* (R Core Team, Vienna).
48. Lé S, Josse J, Husson F (2008) FactoMineR: an R package for multivariate analysis. *J Stat Softw* 25(1):1–18.
49. The MathWorks, Inc. (2013) *Matlab* (The MathWorks, Inc., Natick, MA).
50. de Reuille PB, Bohn-Courseau I, Godin C, Traas J (2005) A protocol to analyse cellular dynamics during plant development. *Plant J* 44(6):1045–1053.
51. The GIMP team (2012) *GNU Image Manipulation Program* (The Free Software Foundation, Boston).
52. Schindelin J, et al. (2012) Fiji: An open-source platform for biological-image analysis. *Nat Methods* 9(7):676–682.
53. Lukšan L, Matonoha C, Vlček J (2009) Algorithm 896: LSA: Algorithms for large-scale optimization. *ACM Trans Math Softw* 36(3):1–29.
54. Johnson SG (2014) *The NLopt Nonlinear-Optimization Package* (MIT, Cambridge, MA).
55. Galassi M, et al. (2009) *GNU Scientific Library Reference Manual* (The Free Software Foundation, Boston), 3rd Ed.
56. Scilab Enterprises (2012) *Scilab: Free and Open Source Software for Numerical Computation* (Scilab Enterprises, Orsay, France).